

## Lattice dynamics in GaN and AlN probed with first- and second-order Raman spectroscopy

U. Haboeck\*, H. Siegle, A. Hoffmann, and C. Thomsen

Technische Universität Berlin, Institut für Festkörperphysik, Sekr. PN 5-4, Hardenbergstr. 36, D-10623 Berlin, Germany

Received 4 March 2003, revised 15 May 2003, accepted 6 June 2003

Published online 28 August 2003

PACS 63.20.Dj, 78.20.-e, 78.30.Fs

We present a selection of our contributions to basic research on the lattice dynamical properties of group-III nitrides and their alloys. We used first-order Raman scattering to determine the zone-center phonons and their dependence on structural attributes such as stress, chemical composition, impurities, and doping. Results on the angular dispersion of the polar modes, strain distribution, coupled LO-phonon plasmon modes, multi-mode behavior in  $\text{Al}_x\text{Ga}_{1-x}\text{N}$ , and the quantitative determination of the phase purity of cubic and hexagonal GaN are shown. Second-order Raman-scattering experiments on GaN and AlN provide information on the vibrational states throughout the entire Brillouin zone. Based on a comparison of experimental data and calculated phonon-dispersion curves we assigned the observed structures to particular phonon branches and points in the Brillouin zone. We also discuss the behavior of the optical modes under large hydrostatic pressure.

© 2003 WILEY-VCH Verlag GmbH & Co. KGaA, Weinheim

**1 Introduction** During the last decade group-III nitrides have been an object of increasing research because of their interesting physical properties such as an adjustable band gap (1.9 eV to 6.2 eV) by varying the composition of the alloys [1] and application as basic materials for optoelectronic devices working in the blue and ultraviolet spectral region [2–4]. In particular GaN and AlN can withstand high temperatures and have large piezoelectric constants which makes them suitable for applications in high-frequency devices, sensors and low-dimensional structures [5, 6].

Although basic information about group-III nitrides e.g. crystal- and band structure have been available for a decade several details still remained unclear. In the following review of our work we present results of first- and second-order Raman investigations on various GaN, AlN, and  $\text{Al}_x\text{Ga}_{1-x}\text{N}$  samples and point out some remarkable details of the structural and optical properties of these materials.

## 2 Experimental

**2.1 Samples** The samples investigated were grown by Hydride Vapor Phase Epitaxy (HVPE), Metal-Organic Vapor Phase Epitaxy (MOVPE), and Molecular Beam Epitaxy (MBE). GaN samples with thicknesses ranging between 200 and 400  $\mu\text{m}$  were grown direct or with a buffer layer on (0001) sapphire substrate using HVPE [7–9]. Their free carrier concentrations (n-type) varied between  $10^{17}$  and  $10^{20} \text{ cm}^{-3}$ . The MOVPE samples, predominantly also n-conducting, were grown with GaN or AlN buffer layers in order to decrease the background carrier concentration [10, 11]; they are only a few  $\mu\text{m}$  thick. The cubic GaN samples were exclusively grown with MBE on (001) GaAs substrates [12, 13]. Their thickness runs from a few nm to 1.8  $\mu\text{m}$  and their free carrier concentrations (n-type) from  $10^{18}$  to  $10^{20} \text{ cm}^{-3}$ . The investigated  $\text{Al}_x\text{Ga}_{1-x}\text{N}$  layers with  $0 < x < 1$  were grown with plasma-assisted MBE on (0001) sapphire and are about 1  $\mu\text{m}$  thick [14, 15]. The AlN samples were fabricated by a direct reaction

\* Corresponding author: e-mail: haboeck@physik.tu-berlin.de, Phone: +49 30 314 24440, Fax: +49 30 314 22064

of aluminum vapor with nitrogen at high temperatures (1900 °C) [16, 17]. These whiskers are some 10  $\mu\text{m}$  thick and up to 1 cm long. Although they are undoped they have background carrier concentrations ranging from  $10^{17}$  up to  $10^{20} \text{ cm}^{-3}$ .

**2.2 Characterization technique** The Raman scattering experiments were carried out using a Dilor XY800 triple-grating spectrometer and a Dilor LABRAM single-grating spectrometer with a super-notch filter. Both systems have a charge-coupled device (CCD) as detector and are equipped with confocal optics. The samples were excited either parallel (in-plane) or perpendicular (on-plane) to the surface using several lines of an  $\text{Ar}^+ - \text{Kr}^+$  mixed-gas laser and the 632.8 nm line of a He–Ne laser. The micro optics focused the laser on a point spot of about 1  $\mu\text{m}$  diameter and detected the scattered light in backscattering geometry, which corresponds to an  $x(\dots)\underline{x}$  configuration for in-plane excitation and a  $z(\dots)\underline{z}$  configuration for on-plane excitation. Spectra have been taken at room temperature and at 4.2 K using an Oxford microscope cryostat. With this setup we obtained a spatial resolution of about 1  $\mu\text{m}$  and a spectral resolution better than  $1 \text{ cm}^{-1}$  for the triple-grating and about  $2 \text{ cm}^{-1}$  for the single-grating spectrometer.

### 3 Results and discussion

**3.1 First-order Raman scattering** We start with the first-order Raman spectra of GaN and AlN that are the basics for further discussion. Under equilibrium growth conditions they both crystallize in the hexagonal wurtzite structure [18] and belong to the point group  $C_{6v}$  (6mm) with four atoms per unit cell. Near  $k = 0$  group theory predicts the following eight modes:  $2A_1 + 2B + 2E_1 + 2E_2$  of which one  $A_1$  and one  $E_1$  correspond to acoustic phonons. The B modes are silent. Because there is no inversion symmetry phonons can be infrared-active as well as Raman-active (i.e., they are polar modes). The Raman-active modes permitted in backscattering geometries<sup>1</sup> of hexagonal GaN and AlN are listed in Table 1.

The corresponding first-order Raman spectra of hexagonal ( $\alpha$ -) GaN and AlN are shown in Fig. 1. The spectra were taken at room temperature with an excitation energy of 632.8 nm in backscattering geometry. The samples  $c$ -axis is parallel to the  $z$ -direction. The  $x$ - and  $y$ -axes are perpendicular to each other and the  $z$ -axis but arbitrary in the  $z$ -plane. Both samples may be considered unstrained because of their bulk-like properties (thick GaN layer, AlN whisker). The Raman modes and scattering geometries are indicated. Forbidden modes which are weakly visible in some spectra originate from non-perfect polarization and scattering geometry or low crystal quality leading to a relaxation of the selection rules. The  $E_1(\text{LO})$  mode is actually not allowed in backscattering geometry but visible in the spectrum taken in  $x(\underline{zz})\underline{x}$  configuration. It likely originates from scattering processes permitted via deformation potential and particularly the Fröhlich interaction. The latter is represented by an electron-phonon interaction Hamiltonian  $H_{ep}$ . The matrix elements of  $H_{ep}$  between an initial and final electronic state taking into account the conservation of  $\mathbf{q}$  lead to two terms. One so-called intraband term is inversely proportional to  $|q|$  and thus singular at  $|q| = 0$ . The other describes interband scattering. Reference [19] shows in detail how both terms can contribute to a ‘forbidden’ LO-scattering.

The phonon frequencies found in our investigations are listed in Table 2. They are in good agreement with other published values [20–24].

**Table 1** First-order Raman modes in wurtzite crystals for different backscattering geometries.

Configuration	Permitted Raman Modes
$z(\underline{xx})\underline{z}$	$E_2(\text{low, high}), A_1(\text{LO})$
$z(\underline{xy})\underline{z}$	$E_2(\text{low, high})$
$x(\underline{zz})\underline{x}$	$A_1(\text{TO}), E_1(\text{LO})$ (see text)
$x(\underline{yy})\underline{x}$	$A_1(\text{TO}), E_2(\text{low, high})$
$x(\underline{yz})\underline{x}$	$E_1(\text{TO})$

<sup>1</sup> Forward scattering, induced by back reflections due to the fact, that the sample is transparent to the laser beam, also occurs.

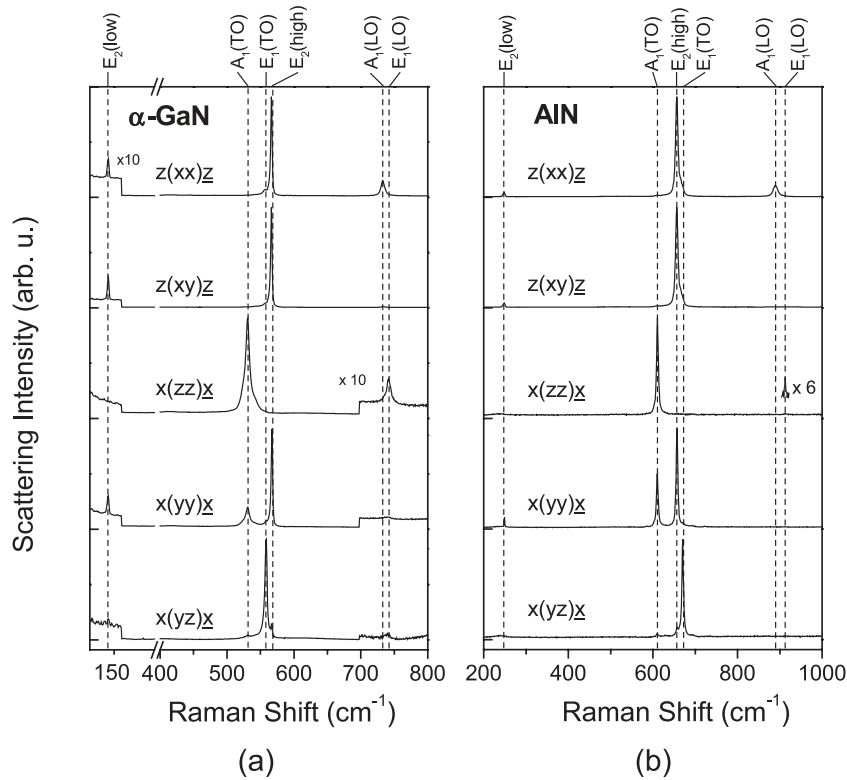


**Fig. 1** Room temperature first-order Raman spectra of hexagonal a) GaN and b) AlN in different scattering geometries normalized to the maximum intensity.

**3.2 Angular dispersion of the polar Raman modes** Since AlN and GaN usually crystallize in the uniaxial hexagonal wurtzite structure the orientation of the  $c$ -axis, which coincides with the optical axis, plays an important role when measuring phonon modes in Raman scattering experiments. A phonon polarized along the optical axis is necessarily an  $A_1$  phonon in this structure, one with a polarization in the plane perpendicular to the optical axis is an  $E_1$  phonon. If the phonon propagation direction is along the crystal axes only purely longitudinal or transverse phonons of well-defined symmetry character are observed in Raman scattering. When the propagation direction is not along one of these axes the frequencies of the polar  $A_1$  and  $E_1$  modes depend on the angular dispersion with respect to the  $c$ -axis and a mixing of the modes, so-called quasi-modes, occurs. Their energy level is located between the high-symmetry modes [25, 26]. If one knows about the angular dispersion the orientation of the  $c$ -axis can be determined.

In uniaxial crystals it is necessary to consider simultaneously two independent forces: the long-range electrostatic forces responsible for the longitudinal-transverse splitting, and the short-range interatomic forces, which reflect the anisotropy of the force constants. For an approximate characterization of the quasi modes wurtzite crystals are divided in two categories [26]: the  $A_1$ – $E_1$  splitting is larger than the LO-TO splitting, i.e., the short-range interatomic forces preponderate the electrostatic forces and the

**Table 2** Frequencies of the first-order Raman modes in hexagonal GaN and AlN at room temperature.

	$E_2(\text{low})$	$A_1(\text{TO})$	$E_1(\text{TO})$	$E_2(\text{high})$	$A_1(\text{LO})$	$E_1(\text{LO})$
GaN	145	533	560	567	735	742
AlN	249	610	669	656	891	912

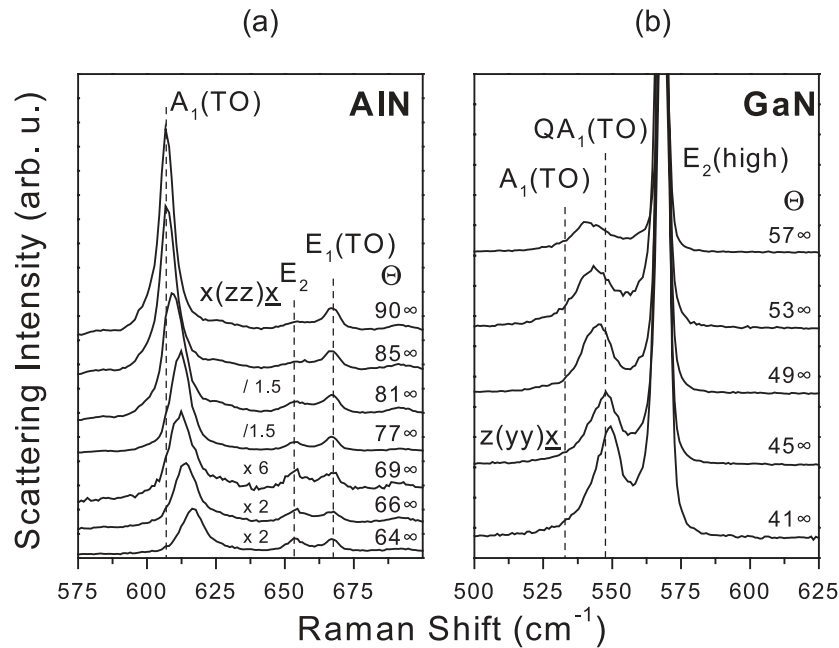


**Fig. 2** Series of Raman spectra for different directions of phonon propagation  $\Theta$  relative to the  $c$ -axis of a) AlN and b) hexagonal GaN. The spectra were taken at room temperature with an excitation energy of 632.8 nm.

quasi modes are a mixture between transverse and longitudinal modes, but still keep their  $A_1$ - or  $E_1$ -symmetry. On the other hand the LO–TO splitting can be much larger than the  $A_1$ – $E_1$  splitting, i.e., the long-range electrostatic forces dominate over the anisotropy of the interatomic forces. The quasi modes then are pure transverse or longitudinal but their symmetry is a mixture of  $A_1$  and  $E_1$ . The latter is the category to which GaN and AlN belong. The energies of the angular-depend LO and TO modes are then given by the equations

$$\omega(\Theta)_{\text{LO}}^2 = \omega_{A_1(\text{LO})}^2 \cos^2(\Theta) + \omega_{E_1(\text{LO})}^2 \sin^2(\Theta), \quad (1)$$

$$\omega(\Theta)_{\text{TO}}^2 = \omega_{A_1(\text{TO})}^2 \sin^2(\Theta) + \omega_{E_1(\text{TO})}^2 \cos^2(\Theta), \quad (2)$$

in which  $\omega(\Theta)$  denotes the frequency of the quasi mode,  $\omega_{E_1}$  and  $\omega_{A_1}$  the frequency of the pure  $E_1$  and  $A_1$  modes, respectively. The LO–TO as well as the  $A_1$ – $E_1$  splitting are listed in Table 3.

In order to compare theoretical calculations (DFT-LDA) such as described in Ref. [27] with experimental data we performed Raman spectroscopy on the AlN whisker crystals described in 2.1 and on a 200  $\mu\text{m}$  thick hexagonal GaN layer grown by HVPE. The spectra plotted in Fig. 2 were taken at room temperature either in backscattering geometry corresponding to  $x(\dots)x$  configuration and in right angle scattering geometry, i.e.,  $z(\dots)z$  configuration.

The samples'  $c$ -axes were tilted with respect to the incident laser beam. From the angle of the incident laser beam and the scattered light relative to the crystal surface we determined the direction of phonon

**Table 3** Comparison between  $A_1$ – $E_1$ -splitting and LO–TO-splitting of GaN and AlN.

	$A_1(\text{LO})$ – $A_1(\text{TO})$	$E_1(\text{LO})$ – $E_1(\text{TO})$	$\gg$	$E_1(\text{LO})$ – $A_1(\text{LO})$	$E_1(\text{TO})$ – $A_1(\text{TO})$
GaN	202 $\text{cm}^{-1}$	182 $\text{cm}^{-1}$	$\gg$	7 $\text{cm}^{-1}$	27 $\text{cm}^{-1}$
AlN	281 $\text{cm}^{-1}$	243 $\text{cm}^{-1}$	$\gg$	21 $\text{cm}^{-1}$	59 $\text{cm}^{-1}$

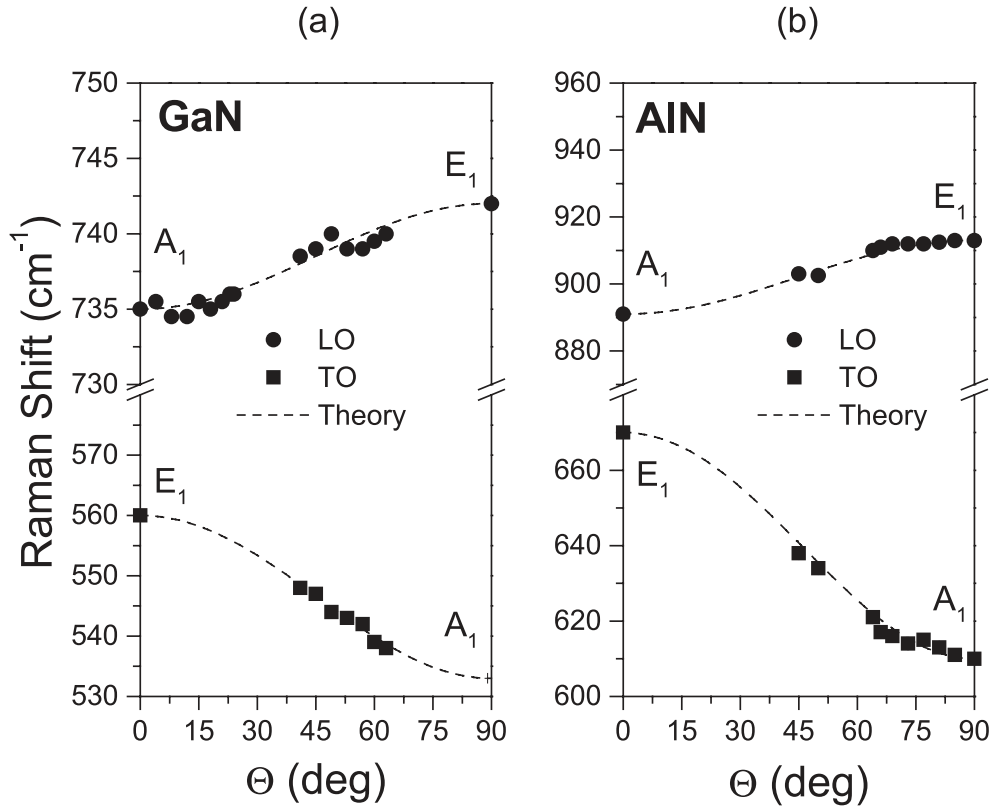


**Fig. 3** Angular dispersion of the LO and TO modes in hexagonal a) GaN and b) AlN for various directions of phonon propagation  $\Theta$  relative to the  $c$ -axis. The dashed lines represent calculations according to equations (1) and (2), the symbols the experimental data.

propagation relative to the optical axis [27]. In the Raman spectra Fig. 2 the shift of the  $A_1(\text{TO})$  and the quasi-TO mode, respectively, caused by the intermixture of the  $E_1$  phonon, towards higher energies is clearly visible. Despite the  $E_2$  and the  $E_1(\text{TO})$  modes are forbidden in  $x(\text{zz})x$  configuration they are weakly detectable because non-perfect crystal structure and polarization alignment (Fig. 2a). They both show no angular dispersion. We point out that the  $E_1(\text{TO})$  phonon does not shift although it is also a polar one. The reason is the double degeneracy of this mode. The crystal has been moved around the  $y$ -axis, i.e., the one  $E_1(\text{TO})$  which is polarized in  $y$ -direction remains unmixed because there is no change with respect to the  $c$ -axis. The second  $E_1(\text{TO})$  polarized in  $x$ -direction mixes with the  $A_1(\text{TO})$  and thus generate the appearance of the quasi mode in the spectra.

Fitting the experimental data with a Lorentzian line shape and plotting it as a function of the phonon propagation direction  $\Theta$  leads to the angular dispersion shown in Fig. 3. The symbols represent the measured energies, the dashed lines the calculated distribution. Because the size and geometry of the samples not all angles could be measured but the experimental data confirm the theoretical prediction quite well: in both GaN and AlN the long range electrostatic forces dominate over the anisotropy of the interatomic forces.

**3.3 Impact of biaxial stress on the vibronic properties** Most of our investigated GaN samples were grown on sapphire. The large mismatch of lattice constant (13.5%) and the different thermal expansion coefficients between hexagonal GaN and sapphire result in a strongly inhomogeneous strain distribution. GaN is biaxially compressively stressed on the sapphire substrate and via the deformation potentials the phonon frequencies change. In hexagonal GaN not all phonon modes are suited for the determination of

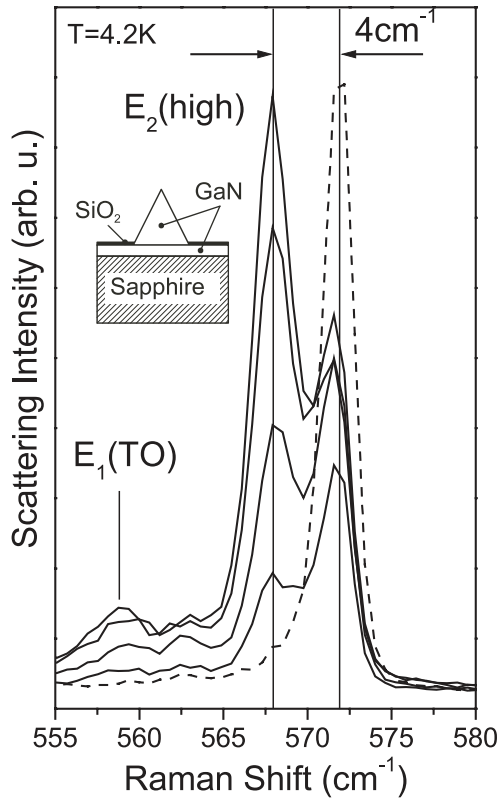


**Fig. 4** Raman spectra of a 10  $\mu\text{m}$  high GaN pyramid grown on sapphire substrate (the sample structure is depicted in the inset). The dashed line shows the spectrum of the strongly compressive strained GaN buffer layer. The solid lines represent spectra taken in different depths of the pyramid.

the strain distribution. As mentioned in 3.2 the polar  $A_1$ - and  $E_1$ -modes show an angular dispersion and thus their frequencies depend on the scattering geometry. The  $E_2(\text{low})$  mode is non-polar and in principle suitable but has a very small pressure coefficient [22]. Hence, the most suited and commonly used line is the  $E_2(\text{high})$ . The phonon shift in case of biaxial (0001)-plane oriented stress can be described by the relation [22]

$$\Delta\omega = K \sigma_{xx = yy}, \quad (3)$$

where  $\sigma_{xx = yy}$  is the component of the stress tensor and  $K$  the pressure coefficient. The values of  $K$  are still a matter of discussion and vary in different publications [28–30]. An overview and discussion is given in the recent work of Wagner and Bechstedt [31].

Figure 4 displays Raman spectra of a 10  $\mu\text{m}$  high GaN pyramid. The structure of the selectively epitaxially grown sample is depicted in the inset, the growth details are given elsewhere [32, 33]. The spectra were recorded spatially resolved with an excitation energy of 514.5 nm at 4.2 K in different sample depths including the top and the GaN-sapphire interface. The latter is the higher-energy dashed line and visualizes the strong compressive stress of about 1 GPa (using the value  $K = 4.2 \text{ cm}^{-1}/\text{GPa}$  [30, 34]) in this region of the sample. The unstressed  $E_2(\text{high})$  frequency is taken to be  $567 \text{ cm}^{-1}$  at room temperature and  $568 \text{ cm}^{-1}$  at 4.2 K, respectively, as determined with measurements on thick ‘quasi-bulk’ samples. Because of the non-perfect scattering geometry a residual  $E_1(\text{TO})$  peak is also detectable. A remarkable result is the gradual decrease in intensity of the  $E_2$  peak from the pyramid together with a corresponding

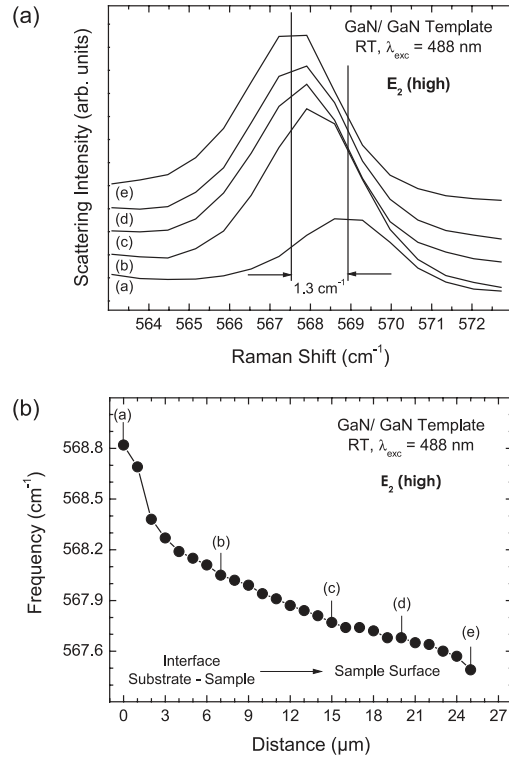


**Fig. 5** (a) Depth profile of a 25  $\mu\text{m}$  thick GaN layer grown on GaN substrate visualizing the shift of the  $E_2(\text{high})$  mode dependent on the distance from the substrate-sample-interface (b)

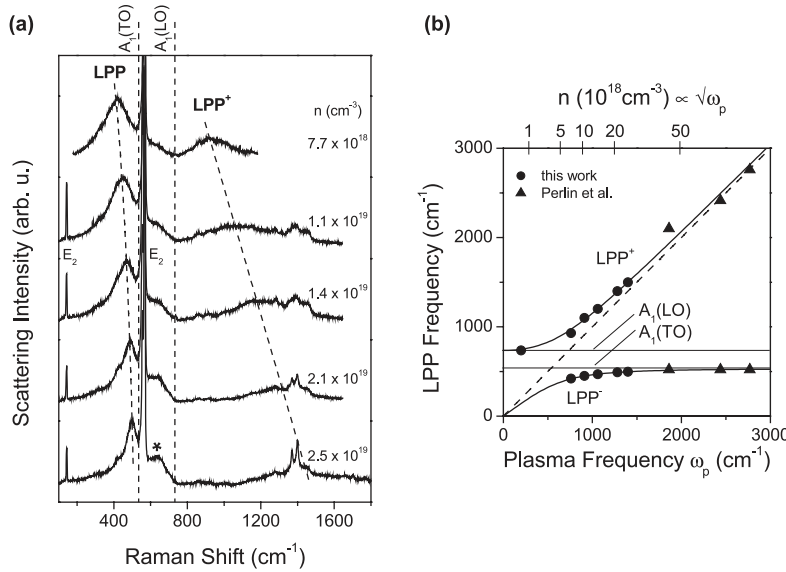


**Fig. 6** a) Raman spectra of MOVPE-grown GaN/sapphire layers having different free-carrier concentrations. The spectra were taken at room temperature in  $z(\dots)\bar{z}$  configuration with  $z$  parallel to the samples  $c$ -axis. Besides the permitted  $E_2$  modes the coupled LO phonon plasmon modes (LPP modes) are observable whereas the also allowed  $A_1(\text{LO})$  phonon disappears. The other structures in the high-energy range originate from second-order scattering and the ruby luminescence of the sapphire substrate. For the peak marked with an asterisk around  $650\text{ cm}^{-1}$  see text. b): Frequency-dependence of the LPP modes on the plasma frequency and the carrier concentration.

increasing in intensity from the peak near the interface without any shift from lower to higher energies, i.e., most of the pyramid is not stressed. The reason is most likely that the ‘freestanding’ GaN of the pyramid is able to expand undisturbed [35].

Usually a step by step relaxation of GaN layers with increasing thickness is observed. Figure 5 represent the result of a spatially resolved line scan at room temperature over a  $25\text{ }\mu\text{m}$  thick GaN layer grown on a GaN template. The stress at the substrate-sample interface is about  $0.4\text{ GPa}$  and thus not as strong as in the above mentioned pyramid which was grown on sapphire. However, there is also a relaxation from the interface towards the surface; in this case we see the expected gradual shift of the  $E_2(\text{high})$  mode.

**3.4 Coupled LO-phonon plasmon modes (LPP modes)** In polar material such as GaN and AlN the macroscopic electric field of the longitudinal-optical phonons can couple to the field of the collective excitation of the free carriers, the so-called plasmons. This results in coupled LO phonon plasmon modes (LPP) [36–39] with one low-energy branch denominated  $\text{LPP}^-$  and a high-energy one called  $\text{LPP}^+$ . The frequencies of this modes depend strongly on the free carrier concentration  $n$ . The dielectric function is composed of a plasmon and a phonon contribution:

$$\varepsilon(\omega) = \varepsilon_\infty \left( 1 - \frac{\omega_p^2}{\omega(\omega + i\gamma)} \right) + \frac{\omega_{\text{LO}}^2 - \omega_{\text{TO}}^2}{\omega_{\text{TO}}^2 - \omega^2 - i\Gamma\omega}, \quad (4)$$

where  $\omega_{\text{LO}}$  and  $\omega_{\text{TO}}$  are longitudinal and transverse optical phonon frequencies, respectively, and  $\varepsilon_\infty$  is the high-frequency dielectric constant.  $\Gamma$  and  $\gamma$  are phonon and electron damping constants.  $\omega_p$  is the uncoupled plasma frequency, defined as

$$\omega_p^2 = \frac{ne^2}{m^* \varepsilon \varepsilon_0}, \quad (5)$$

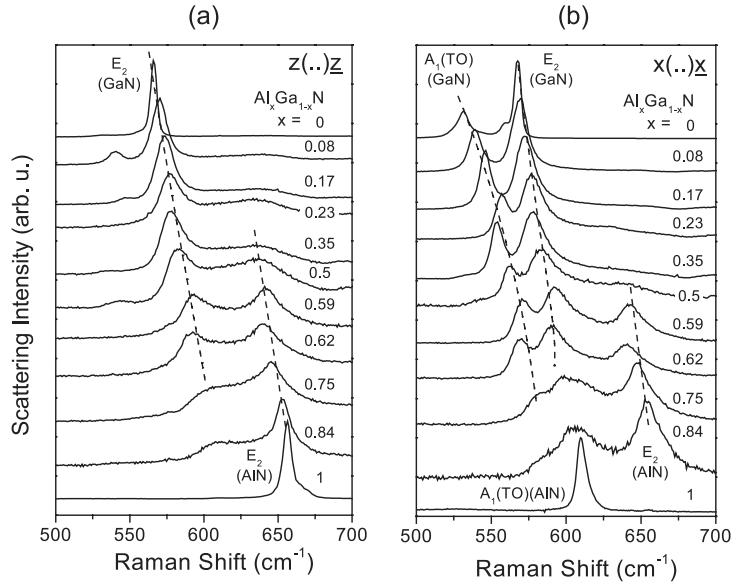


**Fig. 7** Raman spectra of an  $\text{Al}_x\text{Ga}_{1-x}\text{N}$  series with varying Al content ( $0 < x < 1$ ). The spectra are taken at room temperature in (a) on-plane as well as (b) in-plane configuration and are normalized to their maximum intensity. The dashed lines are guide to the eye emphasizing the two-mode-behavior of the  $E_2(\text{high})$  and the  $A_1(\text{TO})$ , respectively.

where  $n$  is the free carrier concentration and  $m^*$  the effective mass of conduction electrons. Neglecting the damping terms, the two LPP frequencies are the roots of the equation:

$$(\omega_{\text{LPP}}^\pm)^2 = \frac{1}{2} \left\{ \omega_{\text{LO}}^2 + \omega_p^2 \pm \left[ (\omega_{\text{LO}}^2 + \omega_p^2)^2 - 4\omega_p^2\omega_{\text{TO}}^2 \right]^{\frac{1}{2}} \right\}. \quad (6)$$

This equation yields the typical non-linear curves plotted in Fig. 6b. In some wide-gap semiconductors such as GaP [40], CdS [41], and SiC [42] LPP-modes could not be observed because of the strong plasmon damping. Some authors also reported on LPP-modes in GaN [39, 43–46] with controversial interpretations. Kozawa et al. [44] only detected the  $\text{LPP}^+$  mode in a small doping range up to  $10^{18}\text{cm}^{-3}$  and deduced an overdamping of the plasmons. In contrast Perlin et al. [39] observed both LPP branches and pointed out that they found no evidence of overdamping. Their measurements were performed on highly doped samples (triangles in Fig. 6b).

With our work [47] we added experimental data in the lower frequency range and furthermore found the dependence of the  $\text{LPP}^-$  mode on the free-carrier concentration  $n$  as visible in the Raman spectra of Fig. 6a. The  $\text{LPP}^-$  exhibits a shift starting at  $420\text{ cm}^{-1}$  up to  $500\text{ cm}^{-1}$  and the  $\text{LPP}^+$  from  $930\text{ cm}^{-1}$  to  $1500\text{ cm}^{-1}$ , respectively. The values are plotted in Fig. 6b (circles) together with those of Ref. [39] and the calculated lineshape according to relation (6). We used  $m^* = 0.2 m_0$  [48],  $\epsilon_\infty = 5.76$  [39], and the frequencies of the  $A_1(\text{TO})$  and  $A_1(\text{LO})$  phonons given in Table 2. Experimental and theoretical data are in good agreement and evidence only a low damping of the plasmon. From the energy position of the LPP-modes we calculated the free-carrier density and assigned them to the corresponding spectra of Fig. 6a. The broader structure at  $650\text{ cm}^{-1}$  marked with an asterisk is also an indication of high carrier density. In Fig. 6a the increasing intensity according to increasing carrier concentration is evident. Demangeot et al. [46] attributed this mode to the  $q$ -dependent electron charge density fluctuation mechanism and concluded a continuous scattering in the TO-LO frequency range activated by the relaxation of  $q$  conserving mirrors the density of LO phonon states renormalized by the interaction with carriers. Knowing about the relation between LPP modes and free carrier concentration Raman spectroscopy can be used as a tool for sample characterization, in particular in inhomogeneous microstructures.



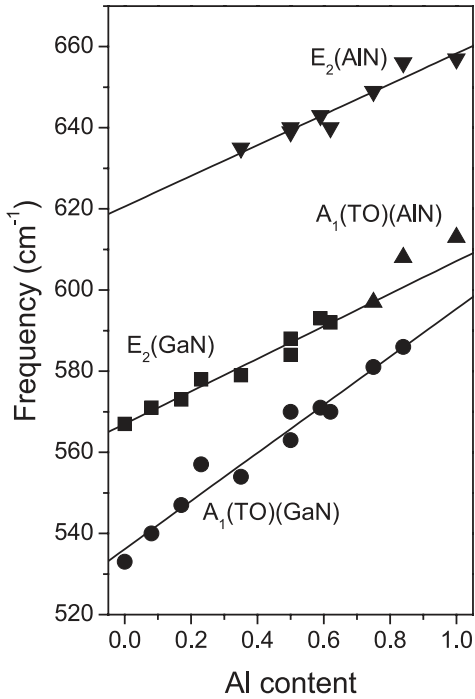


**Fig. 8** Frequencies of phonon modes depending on the Al content of  $\text{Al}_x\text{Ga}_{1-x}\text{N}$ . The circles and rectangles represent GaN-like modes, the triangles those of AlN.

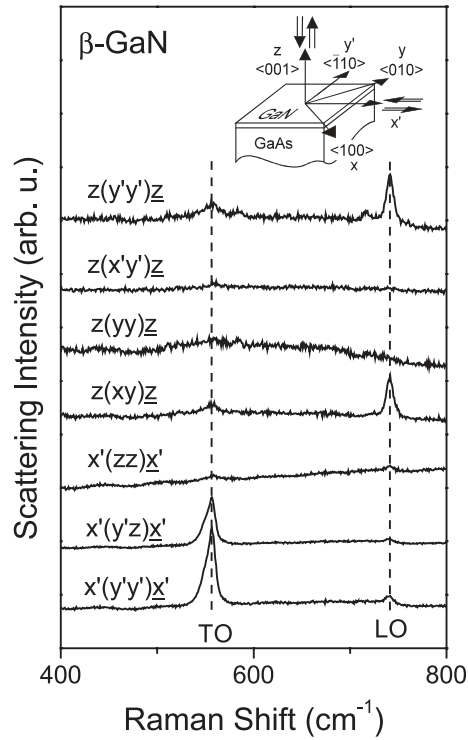


**Fig. 9** Room temperature Raman spectra taken from a cubic GaN sample in various configurations. The inset shows a sketch of the corresponding scattering geometries.

**3.5  $\text{Al}_x\text{Ga}_{1-x}\text{N}$ : dependence of the phonon energies on the Al-content** The phonon frequencies of alloys depend on their stoichiometry in a characteristic way [49–51]: phonons exhibit one- or multi-mode behavior. In the case of one-mode behavior the number of modes does not change with stoichiometry and their frequencies depend approximately linearly on the composition of the alloy. If separate modes of both possible pairs of adjacent atoms exist this is called two-mode behavior, reported e.g. for  $\text{Al}_x\text{Ga}_{1-x}\text{As}$  [52]. Raman measurements on  $\text{Al}_x\text{Ga}_{1-x}\text{N}$  samples with a maximum Al-content of  $x = 0.15$  have been performed by Hayashi et al. [53]. They did not find local modes and deduced a one-mode behavior for  $\text{Al}_x\text{Ga}_{1-x}\text{N}$ . Cros et al. [54] did similar work but over the whole range of Al-contents  $0 < x < 1$ . They observed a one-mode behavior of the  $A_1(\text{LO})$  phonon and a two-mode behavior of the  $E_2(\text{high})$ . We contributed to this with the missing data for the  $A_1(\text{TO})$  phonon. Our results confirmed those of Cros et al. and revealed also a two-mode behavior of the  $A_1(\text{TO})$  phonon.

Figure 7 displays Raman spectra of a series of  $\text{Al}_x\text{Ga}_{1-x}\text{N}$  samples with  $0 < x < 1$  taken at room temperature with an excitation energy of 632.8 nm in (a) on-plane and (b) in-plane configuration. The dashed lines indicate the behavior of the  $E_2(\text{high})$ - and  $A_1(\text{TO})$ -mode as guide to the eye. Comparing both scattering geometries allows the classification of the mode symmetry, i.e.,  $A_1$  or  $E_2$  symmetry. The necessity of such a treatment is visualized in the spectra in Fig. 7b with Al-contents of 0.75 and 0.84 where the AlN- $A_1(\text{TO})$  mode overlap with the GaN-like  $E_2(\text{high})$ . Only a comparison of the different scattering geometries permits the unambiguous identification of the  $A_1(\text{TO})$  character of this mode. The typical broadening of the lines during the transition to a local mode is also discernible. From linear fits of the measured data we obtained

$$A_1(\text{TO})\text{-GaN: } \omega(\text{Al}_x\text{Ga}_{1-x}\text{N}) = 536 \pm 2 \text{ cm}^{-1} + (59 \pm 4 \text{ cm}^{-1}) \cdot x_{\text{Al}}, \quad (7.1)$$

$$E_2(\text{high})\text{-Ga}\text{N}: \quad \omega(\text{Al}_x\text{Ga}_{1-x}\text{N}) = 567 \pm 1 \text{ cm}^{-1} + (40 \pm 3 \text{ cm}^{-1}) \cdot x_{\text{Al}}, \quad (7.2)$$

$$E_2(\text{high})\text{-Al}\text{N}: \quad \omega(\text{Al}_x\text{Ga}_{1-x}\text{N}) = 621 \pm 3 \text{ cm}^{-1} + (38 \pm 4 \text{ cm}^{-1}) \cdot x_{\text{Al}}, \quad (7.3)$$

which gives us a rough estimate for the further characterization of samples with Raman spectroscopy. The advantage of this method over X-ray diffraction measurements is that it can be done spatially resolved and thus detect inhomogeneities or cluster formation. The experimental values together with the linear fits are displayed in Fig. 8.

The absolute error of the samples Al-content was declared to be maximally 5 % by Angerer et al. [15].

**3.6 Determination of the hexagonal minority phase in cubic GaN** Although GaN crystallizes under equilibrium conditions in the hexagonal wurtzite structure improved growth conditions enable the fabrication of the metastable cubic modification. The aim of high carrier mobility in the more easily doped cubic GaN compared to the hexagonal phase [1, 55] has been one of the reasons to focus on this subject. A major difficulty in the growth of cubic ( $\beta$ -) GaN is the polytypism of this material. During the growth process subdomains of hexagonal phases may be built in via a stacking fault mechanism [56]. X-ray measurements showed that cubic domains exist in predominately hexagonal GaN and vice versa [57, 58] whereas the syntactic growth is more dominant in the cubic phase. The standard  $\theta$ - $2\theta$  X-ray scans frequently used to demonstrate the crystal quality are unable to determine a possible minority phase present in a sample. If the  $c$ -axis, e.g., in hexagonal subdomains is tilted by a few degrees with respect to the cubic majority phase only, Bragg peaks originating from the majority phase become observable. Therefore,  $\theta$ - $2\theta$  scans are less suitable for obtaining information about a possible minority-phase content.

Regardless of the particular advantages that one of the two crystal structures of GaN may have over the other, it is important to unambiguously distinguish the two phases when comparing experimental results. Raman spectroscopy is able to verify the purity of GaN layers with respect to polytype-domain formation [59]. The different polarization scattering selection rules allow us to distinguish between the two phases by selecting appropriate scattering geometries. The selection rules for backscattering configurations used in our work is listed in Table 4:

There are two principally different possibilities for the orientation of hexagonal subdomains in cubic GaN. In the first case, the  $c$ -axis [0001] of the hexagonal phase of GaN is tilted only a few degrees with respect to the  $c$ -axis of the otherwise cubic material. In the second case the [0001] axis is parallel to a cubic  $\langle 111 \rangle$  direction, i.e., the space diagonal of the cubic unit cell. In the first case standard  $\theta$ - $2\theta$  X-ray scans are unable to detect hexagonal material. In contrast to the coherent process of X-rays, where the scattering intensity is obtained by the first adding and then squaring, the Raman intensity is the sum of

**Table 4** Raman selection rules for backscattering configurations<sup>1</sup> used in this work (the  $c$ -axis of the cubic GaN is parallel to the  $z$ -direction). The selection rules are only weakly relaxed if the angle between the hexagonal [0001] axis and  $k$  is small.

Surface	Incident Polarization	Scattered Polarization	Porto Notation	Allowed Modes	
				Cubic	Hexagonal
[001]	$[\underline{1}10]$	$[\underline{1}10]$	$z(y'y')\underline{z}$	LO	$E_2, A_1(\text{LO})$
	$[110]$	$[\underline{1}10]$	$z(x'y')\underline{z}$	–	$E_2$
	$[010]$	$[010]$	$z(yy)\underline{z}$	–	$E_2, A_1(\text{LO})$
	$[100]$	$[010]$	$z(xy)\underline{z}$	LO	$E_2$
[110]	$[001]$	$[001]$	$x'(zz)\underline{x}'$	–	$A_1(\text{TO})$
	$[\underline{1}10]$	$[001]$	$x'(v'z)\underline{x}'$	TO	$E_1(\text{TO})$
	$[\underline{1}10]$	$[\underline{1}10]$	$x'(v'y')\underline{x}'$	TO	$A_1(\text{TO}), E_2$

<sup>1</sup> Forward scattering, induced by back reflections due to the fact, that the sample is transparent to the laser beam, also occurs.

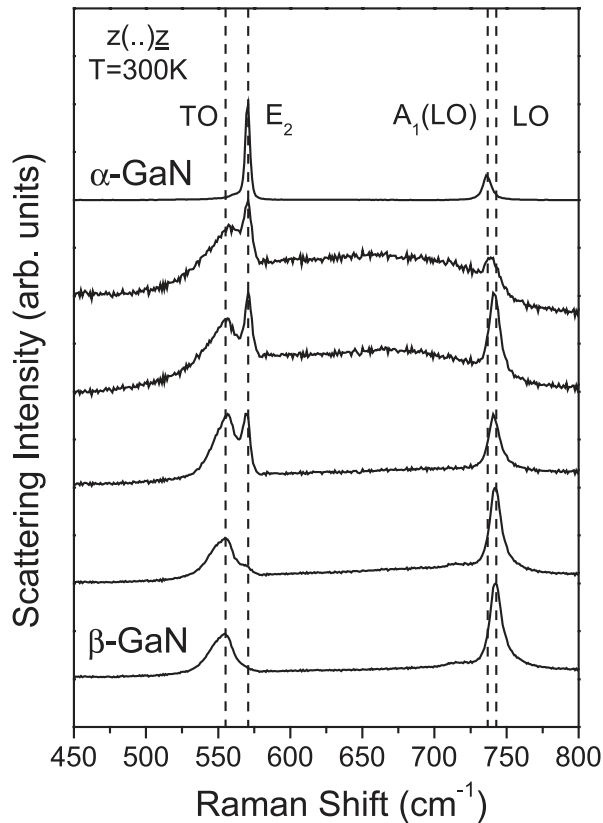


**Fig. 10** Series of GaN samples with top down increasing cubicity. The dashed lines show the position of the hexagonal and cubic phonon modes. For comparable amounts of both phases a broad disorder-activated band between TO and LO mode can be detected.

the squared amplitudes [19, 60]. Therefore, small deviations from principal angles do not affect the Raman scattering intensity significantly, and the minority-phase orientation can be considered as approximately parallel to the cubic phase.

Cubic GaN has zincblende structure and belongs to the point group  $T_d = 43m$  and has thus close to  $k=0$  a doubly degenerate TO and a single LO phonon with a higher frequency. The wurtzite material may be considered having a slightly distorted zincblende structure in nearest neighbor distance; consequently the energy difference between the Raman modes of both phases are not very large and make it difficult to determine the minority-phase content. The frequencies of the hexagonal phase are given in Table 2. Those of the cubic phase obtained by the Raman spectra displayed in Fig. 9 are  $\omega_{\text{TO}} = 555 \text{ cm}^{-1}$  and  $\omega_{\text{LO}} = 740 \text{ cm}^{-1}$ .

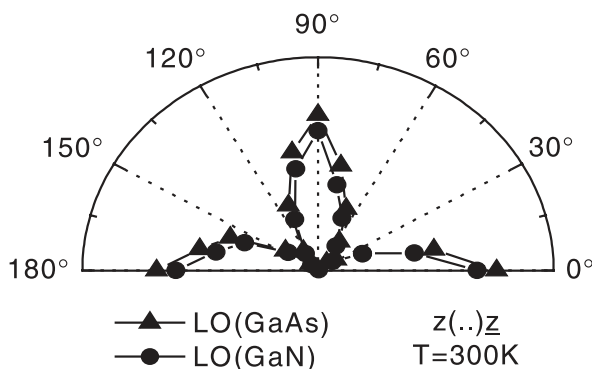


**Fig. 11** Polarization dependence of the parallel polarized GaN and GaAs LO-phonon intensity as the sample is rotated. An angle of  $45^\circ$  corresponds to  $z(yy)z$ .

These values agree well with the results of other workers [61, 62]. As can be seen from Tab. 4 it is possible to distinguish the two phases of GaN using the  $z(\dots)\bar{z}$  configuration because of the different selection rules of the cubic LO and the hexagonal  $A_1(\text{LO})$  mode in spite of their closeness in frequency. While in  $z(y'y')\bar{z}$  configuration both modes are observable, in the  $z(yy)\bar{z}$  (rotated by  $45^\circ$  in the polarization plane) only the hexagonal  $A_1(\text{LO})$  mode is allowed. To compare the lines originating from cubic or hexagonal GaN we investigated a series of samples with different degrees of cubicity. Figure 10 shows the corresponding Raman spectra.

Even the slightly different phonon frequencies (vide the shift of the  $A_1(\text{LO})$  towards the LO frequency) and particularly the  $E_2$ -mode, which does not appear in cubic material, make it possible to estimate the phase purity of the samples. This becomes more difficult the less hexagonal material is built in. To determine the phase purity of GaN samples using the  $z(\dots)\bar{z}$  configurations one has to be sure of the epitaxial growth of the investigated layer. For a cubic GaN layer oriented only in growth direction but not perpendicular to it there is obviously no selection rule involving  $x$ - and  $y$ -polarizations. In order to estimate the cubicity quantitatively we fitted a Lorentzian to the allowed polarization ( $y'y'$ ) and compared it to the spectrum in  $yy$ -polarization. For the sample which spectra are shown in Fig. 9 we found a cubicity of better than 98% (having corrected for the different thicknesses and relative Raman coefficients). An unambiguous method for the quantitative determination of the cubicity is obtained for Raman excitation in plane of the substrate. By comparing the  $x'(zz)\bar{x}'$  and  $x'(y'y')\bar{x}'$  configuration the hexagonal phase content can easily be determined. The  $E_1(\text{TO})$  phonon which appears nearly at the same frequency as the cubic TO mode is forbidden in the  $x'(y'y')\bar{x}'$  configuration. Therefore comparing the intensity ratio as described above of the cubic TO and the hexagonal  $E_2(\text{high})$  mode, which are furthermore separated more than  $10\text{ cm}^{-1}$  from each other, allows the determination of the sample's cubicity.

In the second case the  $[0001]$  axis is parallel to a cubic  $\langle 111 \rangle$  direction, i.e., the space diagonal of the cubic unit cell. Even then it is difficult to detect the hexagonal minority phase with  $\theta$ - $2\theta$  X-ray scans whereas in Raman measurements an  $E_2$ -signal is available in all configurations mentioned so far. In order to obtain quantitative information we measured the polarization dependence of the phonon modes of a cubic sample. Figure 11 shows polar plots of the intensity of the LO phonon mode of GaN compared to the LO mode of GaAs. The incident and scattered polarizations were kept fixed and parallel polarized, while the sample was rotated in total by  $180^\circ$  in the plane defined by the polarizations. The GaN mode exhibits the same polarization dependence as the GaAs mode indicating an epitaxial growth. If both phases coexisted in the sample, the different polarization dependences would overlap and the distinct  $d$ -wave like minima of the scattering intensity would disappear with increasing hexagonal-phase content.

**3.7 Zone-boundary phonons in GaN and AlN** In contrast to first-order Raman measurements second-order experiments provide information on the vibrational states throughout the entire Brillouin zone, which is important in considering, for example, the electronic conduction or nonradiative relaxation processes of electrons. An earlier publication about second-order Raman scattering on GaN was done by Murugkar et al. [63]. They investigated only hexagonal GaN for frequencies higher than  $1280\text{ cm}^{-1}$ . Our measurements on hexagonal and cubic GaN covered the spectral region from  $200\text{ cm}^{-1}$  until  $1550\text{ cm}^{-1}$  and thus contain the acoustic as well as the optical overtone and combination part. We used all necessary scattering geometries to obtain selection rules and performed a calculation of the dispersion curves [64, 65]. In order to derive the selection rules for second-order Raman scattering we carried out a group-theoretical analysis. Using these selection rules in addition to the calculated dispersion curves we assigned the observed peaks of GaN and AlN to particular phonon branches and determined the points in the Brillouin zone from which the scattering originates.

To calculate the phonon dispersion of hexagonal GaN we used a modified valence-force model of Kane [66] which is detailed in Ref. [65]. By adjusting our model to results of *ab initio* calculations [67, 68] we obtained corresponding results. Figure 12 displays the phonon dispersion of hexagonal GaN and AlN.

The phonon dispersion is related to the phonon density of states. The latter is reflected by the second-order intensity since phonons with wave vectors throughout the whole Brillouin zone are involved. The various structural characteristics of the second-order spectra are due to variations in the density of pho-

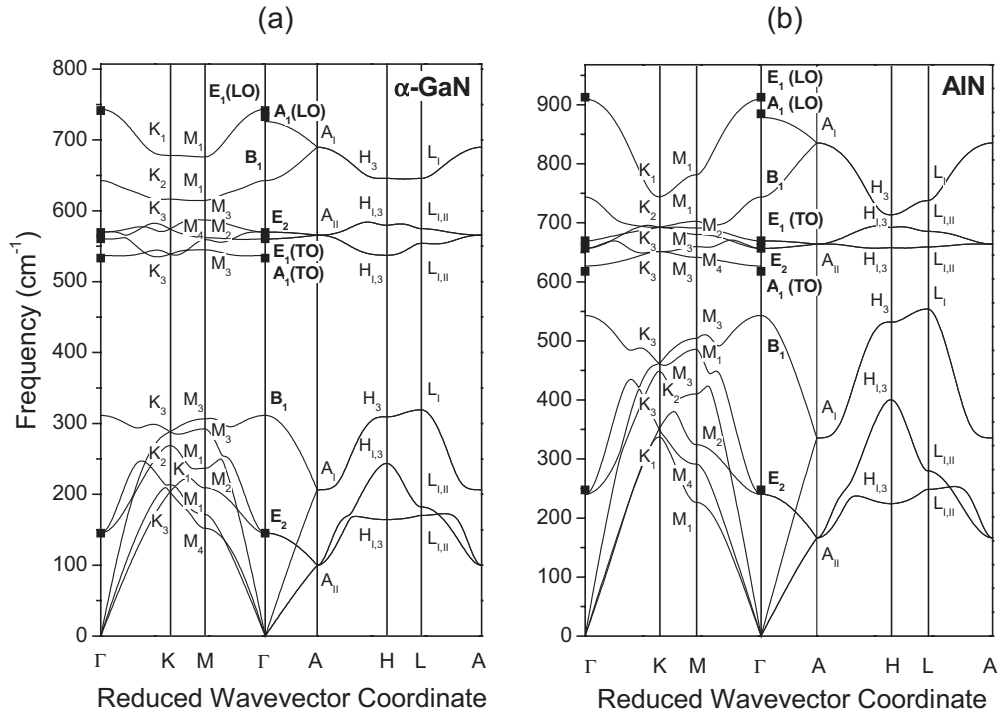


**Fig. 12** Calculated phonon-dispersion curves for a) hexagonal GaN and b) AlN.

non states and selection rules for various scattering processes (combinations and overtones). From the results of our group-theoretical analysis the following conclusions can be drawn (for details vide Ref. [65]):

Overtones always contain the representation  $A_1$  while combinations of phonon states belonging to different irreducible representations never contain  $A_1$ .

More overtones or combinations become allowed with decreasing symmetry of the point in the Brillouin zone considered.

A consequence of the different packing sequence of hexagonal GaN (ABAB) compared to the cubic material (ABCABC) is halving the Brillouin-zone dimension in the cubic (111) direction, which is followed by a folding of the phonon branches at the new zone boundary. Frequencies which previously occurred at the symmetry point L in the zinc-blende Brillouin zone now occur at the center of the wurtzite Brillouin zone. Hence, the different phonon branches from the  $\Gamma$  point, e.g. the optical  $\Gamma_6 = E_2$  and the acoustic  $\Gamma_3 = B$  run together at the A point. Therefore, we use  $A_I = A_1 + A_3$  and  $A_{II} = A_5 + A_6$ . The same applies to the points H and L.

It is important to point out that, apart from the selection rules, the density of two-phonon states determines the intensity of the second-order Raman signal [19]. Figure 13 shows an overview of a room temperature Raman spectrum of a hexagonal and a cubic GaN layer which exhibit a rich structure due to second-order scattering processes beside those known to be first-order originated. The samples were excited either perpendicular or parallel to the sample surface depending on the scattering geometry using the 632.8 nm line of a He–Ne laser and the 514.53 nm line of an  $\text{Ar}^+$  laser. The scattered light was detected in backscattering geometry which corresponds to either an  $x(\underline{zz})\underline{x}$  ( $A_1$ ), an  $x(\underline{yz})\underline{x}$  ( $E_1$ ), or a  $z(\underline{xy})\underline{z}$  ( $E_2$ ) configuration.

The total spectrum may be divided into three parts: the low-frequency region (200–650  $\text{cm}^{-1}$ ) is dominated by acoustic overtones; optical and acoustic combination bands appear below and above the first-order optical scattering (650–1000  $\text{cm}^{-1}$ ); and, finally, the second-order optical bands in the high-frequency range (1000–1500  $\text{cm}^{-1}$ ). The corresponding spectra taken from the hexagonal GaN sample in

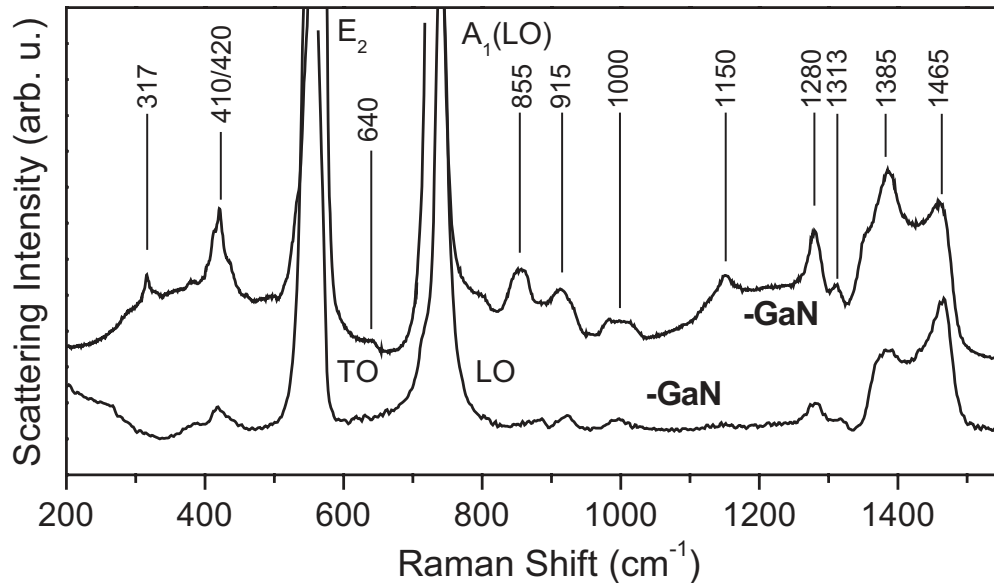


**Fig. 13** Second-order Raman spectrum of hexagonal ( $\alpha$ -, upper curve) and cubic ( $\beta$ -, bottom curve) GaN grown on (0001) sapphire and (001) GaAs, respectively. The spectra were recorded at room temperature in backscattering geometry, corresponding to  $z(\dots)\bar{z}$ .

$A_1$ ,  $E_1$ , and  $E_2$  scattering geometry are shown in Fig. 14. In the following the strongest experimentally observed structures along with our calculated phonon-dispersion curves (Fig. 12) will be discussed and compared to the modes observed in cubic GaN. Recently, inelastic x-ray scattering has become an interesting technique for studying the phonon dispersion throughout the Brillouin zone [69]. When we compare our calculated dispersion curves with these experiments we find an, in general, excellent agreement. Differences arise in the splitting of  $B_1$  and LO-derived branches which in our model is larger by a factor of about 2 compared to the one in Ref [69]. For details see Fig. 12 and Ref. [69] where the experimental work is compared to *ab initio* calculations and the results of [65, 70, 71].

The low-frequency region displayed in Fig. 14a exhibits two strong Raman bands, one located at  $317\text{ cm}^{-1}$  and a doublet at  $410/420\text{ cm}^{-1}$ . Whereas the  $317\text{ cm}^{-1}$  and the  $410\text{ cm}^{-1}$  modes unambiguously have  $A_1$  symmetry the  $420\text{ cm}^{-1}$  line also shows  $E_2$  symmetry (see inset of Fig. 14a). From the lineshape and its low frequency we assign the  $317\text{ cm}^{-1}$  mode to an overtone process of acoustic phonons. As can be seen in the phonon dispersion (Fig. 12) the energy as well as the observed symmetry fits well with the flat branch at the H point in the Brillouin zone. This is emphasized by the fact that this mode was not observed in cubic GaN. The doublet at  $410/420\text{ cm}^{-1}$  is also due to acoustic phonons. Comparing the phonon-dispersion curves (Fig. 12) it can be attributed to an overtone of transverse-acoustic phonons either at the symmetry point A, K, or M. According to the selection rules the part of the doublet having pure  $A_1$  symmetry, i.e., the  $410\text{ cm}^{-1}$  line, is assigned to originate from the A or K point whereas the  $420\text{ cm}^{-1}$  mode having  $A_1$  and  $E_2$  symmetry belongs to the M point. The last mode of the low-frequency region lying between the first-order modes at around  $640\text{ cm}^{-1}$  can be attributed to an overtone process of the highest acoustic-phonon branch either at the zone boundary (L point) or from the B mode at the  $\Gamma$  point. The middle-frequency region is dominated by three modes which we attribute to combinations between acoustic and optical phonons considering the phonon-dispersion and the fact that most of them are found in the spectra of the cubic sample, too. Overtones can be excluded because of the gap between the acoustic- and optical-phonon branches which extends in the overtone spectrum from approximately  $650\text{--}1050\text{ cm}^{-1}$ . The optical combination and overtone region is shown in Fig. 14c. Most of the modes are strongest in  $A_1$  symmetry. The structure located at  $1150\text{ cm}^{-1}$  is probably a consequence of the flat dispersion curve of GaN in the energy region between the  $A_1(\text{TO}) = 533\text{ cm}^{-1}$  and  $E_2 = 569\text{ cm}^{-1}$ . From

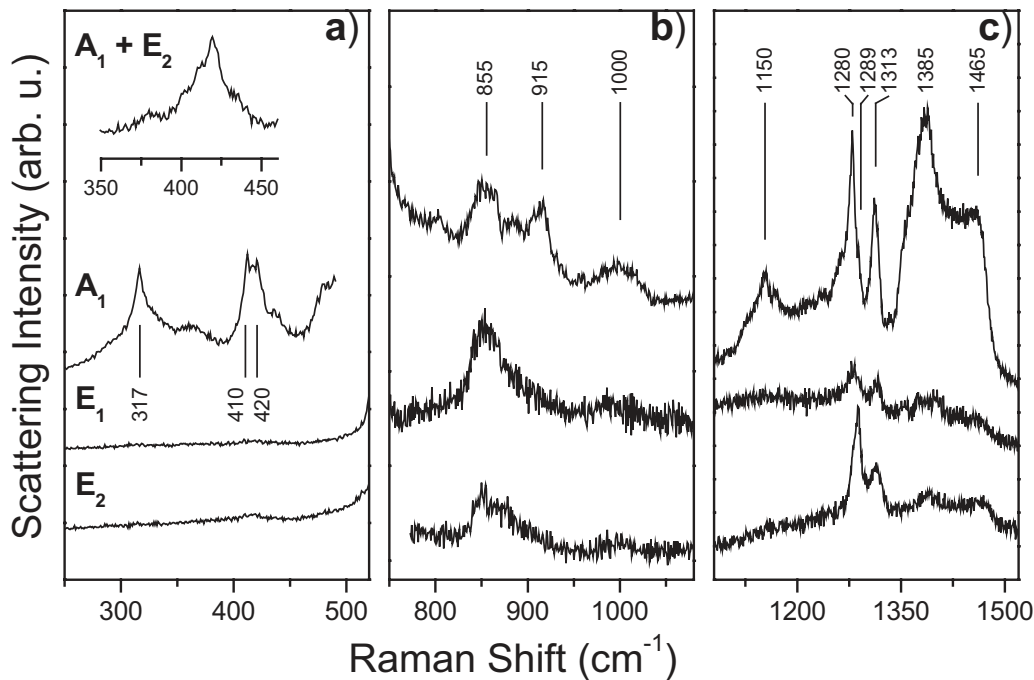


**Fig. 14** Second-order Raman spectra of hexagonal GaN taken at room temperature for various scattering geometries corresponding to symmetry  $A_1$ ,  $E_1$ , and  $E_2$  in the a) low-, b) middle-, and c) high-frequency region.

**Table 5** Frequencies and symmetries of the strongest modes found in the first- and second-order Raman spectra of hexagonal GaN and their assignments.

Frequency ( $\text{cm}^{-1}$ )	Symmetry	Process	Point in the BZ
317	$A_1$	acoustic overtone	H
410	$A_1$	acoustic overtone	A, K
420	$A_1, E_2$	acoustic overtone	M
533	$A_1$	first-order process	$\Gamma = A_1(\text{TO})$
560	$E_1$	first-order process	$\Gamma = E_1(\text{TO})$
567	$E_2$	first-order process	$\Gamma = E_2(\text{high})$
640	$A_1$	overtone	$\Gamma = [\text{B}]^2, \text{L}$
735	$A_1$	first-order process	$\Gamma = A_1(\text{LO})$
742	$E_1$	first-order process	$\Gamma = E_1(\text{LO})$
855	$A_1, E_1, E_2$	acoustic-optical comb.	
915	$A_1$	acoustic-optical comb.	
1000	$A_1, (E_2)$	acoustic-optical comb.	
1150	$A_1$	optical overtone	
1280	$A_1, (E_1)$	optical combination	
1289	$E_2$	optical combination	
1313	$A_1, (E_1, E_2)$	optical combination	
1385	$A_1$	optical combination	A, K
1465	$A_1$	optical overtone	$\Gamma = [A_1, \text{LO}]^2$
cutoff 1495	$A_1, E_2$	optical overtone	$\Gamma = [E_1, \text{LO}]^2$

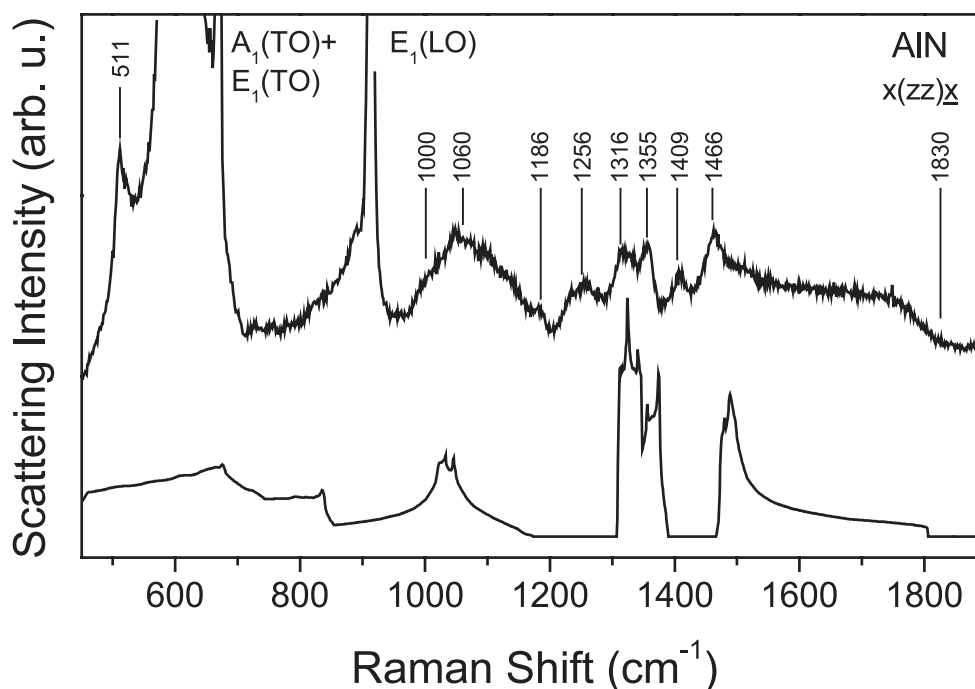


**Fig. 15** Second-order Raman spectrum of hexagonal AlN taken at room temperature in backscattering geometry, corresponding to  $x(\dots)x$  (upper curve) and calculated overtone phonon density (bottom curve) of cubic AlN [67].

the observed  $A_1$  symmetry we consider an optical overtone most likely originating from the H point. The narrow peaks at 1280 and 1313  $\text{cm}^{-1}$  are most intensive in  $A_1$  symmetry but they also appear in the  $E_1$  spectrum. In the  $E_2$  spectrum the 1313  $\text{cm}^{-1}$  mode is likewise visible but instead of the 1280  $\text{cm}^{-1}$  peak a mode appears at 1289  $\text{cm}^{-1}$ . Despite the fact that combinations of zone-center modes are possible from energy considerations we assign them to combination processes at the zone boundary because of the observed symmetry and their appearance in the cubic spectrum, too. The highest-energy distribution with a cutoff at 1495  $\text{cm}^{-1}$  is attributed to an overtone of the zone-center  $E_1(\text{LO})$  mode according to the observed symmetry. The upper maximum of the camelback structure at around 1465  $\text{cm}^{-1}$  corresponds to an overtone of the zone-center  $A_1(\text{LO})$  mode. The lower camelback at 1385  $\text{cm}^{-1}$  arises from the highest phonon branches which become flat at the Brillouin boundary. Hence, they originate either from the A or K point. The frequencies of the observed first- and second-order features together with their symmetry and their assignments are listed in Table 5.

The last item of this paragraph about the results of second-order scattering will be on AlN. Figure 15 exhibits a room temperature Raman spectrum of hexagonal AlN (upper curve) together with a calculated density of two-phonon states [67] of cubic AlN (bottom curve).

The gap between the acoustic and the optical phonon branches of AlN amounts only to about 60  $\text{cm}^{-1}$  and is thus much smaller than that of GaN (see also Fig. 12) because of the smaller mass difference between Al and N compared to Ga and N. A classification of frequency regions with absolute acoustic or optical character as done above for GaN is therefore not possible. According to Fig. 12 acoustic overtones can occur until approx. 1100  $\text{cm}^{-1}$ . Optical combinations and overtones are expected from 1220  $\text{cm}^{-1}$  on. Acoustic-optical combinations can appear in a broad overlap region. Figure 16 shows the full Raman spectra of a hexagonal AlN sample in the relevant  $A_1$ ,  $E_1$  and  $E_2$  configuration. In the following we discuss the strongest structures in comparison with the calculated phonon dispersion (Fig. 12) and the density of two-phonon states (Fig. 15) and assign them according to the selection rules of second-order scattering.



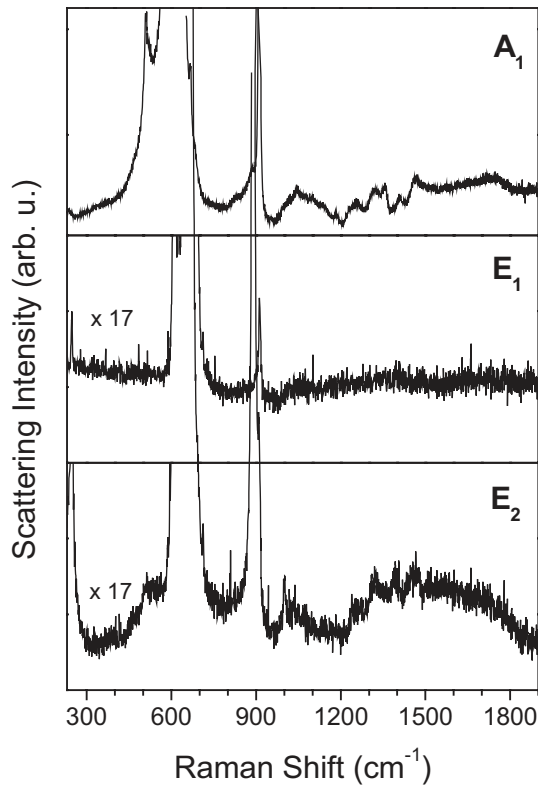


**Fig. 16** Second-order Raman spectra of hexagonal AlN taken at room temperature for various scattering geometries corresponding to symmetry  $A_1$ ,  $E_1$ , and  $E_2$ , respectively.

Below the first-order Raman modes a sharp line appears at  $511\text{ cm}^{-1}$  in the spectrum with  $A_1$  symmetry whereas only a broad structure is visible in  $E_2$  symmetry. In the latter the structure seems to be split into two with maxima at  $511$  and  $553\text{ cm}^{-1}$ . Whether the line at  $553\text{ cm}^{-1}$  has even  $A_1$  symmetry or not cannot be deduced from the spectra because of its overlap with the strong peak of the first-order  $A_1(\text{TO})$  mode. Comparing the calculated phonon dispersion (Fig. 12) one finds that the energies possible due to the symmetry differ from the experimental data. Comparing the spectra with those of GaN we find a similarity to the lineshape of the structure at  $317\text{ cm}^{-1}$  and thus assign the line at  $511\text{ cm}^{-1}$  in the spectrum of AlN to the flat running acoustic phonon branch of the H point. This is supported by the fact that it is not visible in the calculated cubic overtone density. Due to the above mentioned difficulty to

determinate the symmetry of the shoulder at  $553\text{ cm}^{-1}$  an unambiguous assignment is not possible. It might result from a combination, overtone or difference process from the M point.

**Table 6** Frequencies and symmetries of the strongest modes found in the first- and second-order Raman spectra of hexagonal AlN and their assignments.

Frequency ( $\text{cm}^{-1}$ )	Symmetry	Process	Point in the BZ
511	$A_1, (E_2)$	acoustic overtone	H
553	$E_2, (A_1)$		M
610	$A_1$	first-order process	$\Gamma = A_1(\text{TO})$
656	$E_2$	first-order process	$\Gamma = E_2(\text{high})$
669	$E_1$	first-order process	$\Gamma = E_1(\text{TO})$
891	$A_1$	first-order process	$\Gamma = A_1(\text{LO})$
912	$E_1$	first-order process	$\Gamma = E_1(\text{LO})$
1000	$E_2, (A_1)$	acoustic overtone	M
1060	$A_1, E_2$	acoustic overtone, comb.	M
1186	$A_1, E_2$	acoustic-optical comb.	M
1256	$A_1, E_2$		M
1316	$A_1, E_2$	optical overtone	$\Gamma = [E_2]^2$
1355	$A_1$	optical overtone	K, H
1393	$E_2$	optical combination	M
1409	$A_1$	optical overtone	K, H
1466	$A_1$	optical overtone	$\Gamma, K$
cutoff 1830	$A_1, E_2$	optical overtone	$\Gamma = [E_1]^2$

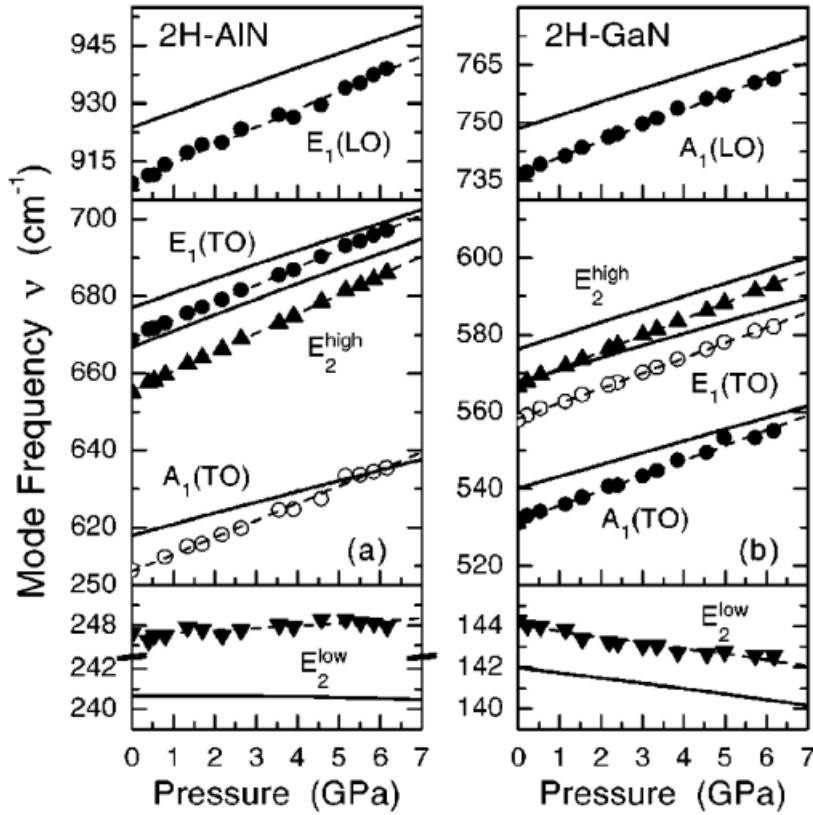


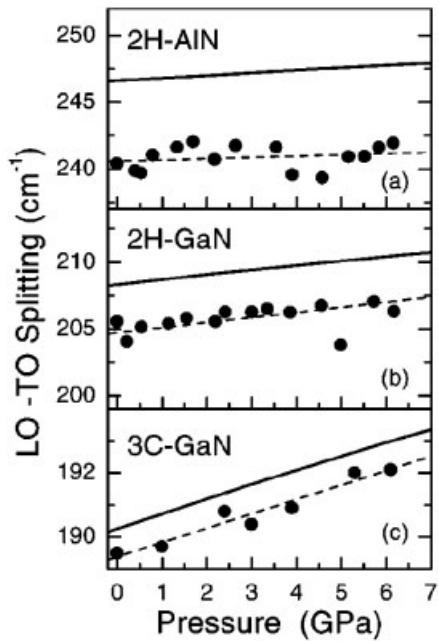
**Fig. 17** Measured zone center optical phonon frequencies (symbols) versus hydrostatic pressure for 2H-AlN (left panels) and 2H-GaN (right panels). Solid lines represent the results of *ab initio* calculations. Dashed lines are linear fits to the experimental data.

Beyond the first-order phonons a broad structure appears at around  $1060\text{ cm}^{-1}$  having  $A_1$  and  $E_2$  symmetry. Additionally a sharp peak at  $1000\text{ cm}^{-1}$  is detected in the  $E_2$  symmetry. Comparing this with the calculated overtone density leads to the assignment to originate from the M point. The energy of the peak at  $1186\text{ cm}^{-1}$  is located in the gap between the acoustic and optical branches and must thus stem from an acoustic optical combination process. Because of the observed  $A_1$  and  $E_2$  symmetry it originates most likely from the M point. Considering the calculated phonon dispersion the structure at around  $1256\text{ cm}^{-1}$  can be explained as an acoustic-optical combination ( $M_1 \times M_1$  with  $\omega_{\text{calc}} = 1267\text{ cm}^{-1}$ ) as well as an optical overtone ( $[M_3]^2$  with  $\omega_{\text{calc}} = 1276\text{ cm}^{-1}$ ). Both processes fulfill the selection rules. Davydov et al. suggested an optical overtone from the K or M point [70]. The doublet at  $1316$  and  $1355\text{ cm}^{-1}$  is assigned to optical overtones; the first one at  $1316\text{ cm}^{-1}$  having  $A_1$  and  $E_2$  symmetry coincides with the double  $E_2(\text{high})$  energy of the first-order scattering and is hence its overtone. The structure at about  $1400\text{ cm}^{-1}$  is composed of one line at  $1409\text{ cm}^{-1}$  with pure  $A_1$  symmetry and a second line at  $1393\text{ cm}^{-1}$  with defined  $E_2$  symmetry. The latter we assign because of its symmetry to a  $M_1 \times M_2$  process ( $\omega_{\text{calc}} = 1394\text{ cm}^{-1}$ ) whereas the lines at  $1409$  and  $1355\text{ cm}^{-1}$  do not allow an unambiguous classification. Overtones originating from the K or H point are possible. The last well resolved peak at  $1466\text{ cm}^{-1}$  visible in  $A_1$  symmetry we consider to be an optical  $K_1$  or  $B_1$  overtone. Hence, we obtain the frequency of the silent  $B_1$  [ $\Gamma$ ] mode to be  $733\text{ cm}^{-1}$  what fits to the *ab-initio* calculations of Gorczyca et al [72]. Davydov et al. found this structure in  $A_1$  and  $E_2$  symmetry and assigned it to an optical combination process from the M point [70]. The cutoff at around  $1830\text{ cm}^{-1}$  is attributed analogous to GaN to an overtone of the zone-center  $E_1(\text{LO})$  mode according to the observed symmetry. All phonon frequencies together with their symmetries and assignments are listed in Table 6.

**Table 7** Fitting parameters used for the pressure dependence of the phonon frequencies in GaN and AlN and resulting Grüneisen parameters  $\gamma$ .

mode	$\omega$ (cm <sup>-1</sup> )		$\partial\omega/\partial P$ (cm <sup>-1</sup> /GPa)		$\gamma$	
	Expt.	Calc.	Expt.	Calc.	Exper.	Calc.
2H-AlN						
E <sub>2</sub> (low)	247.5 ± 0.5	241	0.12 ± 0.05	-0.03	0.10 ± 0.05	-0.02
A <sub>1</sub> (TO)	608.5 ± 0.5	618	4.4 ± 0.1	3.0	1.51 ± 0.05	1.02
E <sub>2</sub> (high)	655.5 ± 0.1	667	4.99 ± 0.03	4.2	1.58 ± 0.01	1.34
E <sub>1</sub> (TO)	669.3 ± 0.1	677	4.55 ± 0.03	3.8	1.41 ± 0.01	1.18
A <sub>1</sub> (LO)	891	898		3.5		0.82
E <sub>1</sub> (LO)	910.1 ± 0.4	924	4.6 ± 0.1	4.0	1.06 ± 0.03	0.91
2H-GaN						
E <sub>2</sub> (low)	144.1 ± 0.2	142	-0.3 ± 0.1	-0.24	-0.4 ± 0.1	-0.35
A <sub>1</sub> (TO)	531.7 ± 0.3	540	3.9 ± 0.1	3.1	1.47 ± 0.04	1.21
E <sub>1</sub> (TO)	558.2 ± 0.1	568	3.94 ± 0.03	3.3	1.41 ± 0.01	1.19
E <sub>2</sub> (high)	567.0 ± 0.1	576	4.24 ± 0.03	3.6	1.50 ± 0.01	1.28
A <sub>1</sub> (LO)	736.5 ± 0.2	748	4.4 ± 0.1	3.5	1.20 ± 0.05	0.98
E <sub>1</sub> (LO)	742 ± 0.2	757		3.6		0.99
3C-GaN						
TO	553 ± 2	560	4.0 ± 0.2	3.2	1.4 ± 0.1	1.19
LO	743 ± 2	750	4.5 ± 0.2	3.7	1.20 ± 0.05	1.02

**3.8 Lattice vibrations under hydrostatic pressure** Aside from work on the optical transitions [73] and the local vibrational modes of Mg [74] under pressure and for different temperatures, we also studied the effect of pressure on the optical phonon frequencies in GaN and AlN. This work which contains experiments and *ab initio* work focuses on the possible softening of the E<sub>2</sub>(low) mode under pressure and on the effective charge as defined by the splitting of TO and LO modes. The experiments were performed on hexagonal GaN grown on SiC and on AlN whiskers. The samples were pressurized in a dia-

**Fig. 18** Experimental LO-TO splittings (symbols) as a function of pressure for a) the 2H-AlN E<sub>1</sub> modes, b) the 2H-GaN A<sub>1</sub> modes, and c) 3C-GaN. Solid lines represent the results of *ab initio* calculations. Dashed lines are linear fits to the experimental data.

**Table 8** Pressure coefficients of the LO–TO splitting  $\Delta\omega$  and transverse effective charge  $e_T^*$  (in units of the elementary charge  $e$ ).

material	mode	$\Delta\omega$ (cm <sup>-1</sup> )		$\partial(\Delta\omega)/\partial P$ (cm <sup>-1</sup> /GPa)		$e_T^*$ (e)		$\partial e_T^*/\partial P$ (10 <sup>-3</sup> e/GPa)	
		Expt.	Calc.	Expt.	Calc.	Expt.	Calc.	Expt.	Calc.
2H-AlN	E <sub>1</sub>	240.8 ± 0.5	247	0.10 ± 0.12	0.21	2.63 ± 0.05	2.54	0.15 ± 0.70	-1.0
2H-GaN	A <sub>1</sub>	205.3 ± 0.2	208	0.4 ± 0.1	0.39	2.73 ± 0.03	2.74	-1.3 ± 07	-2.0
3C-GaN	(cub.)	189 ± 1	190	0.45 ± 0.05	0.50	2.65 ± 0.03	2.65	0.0 ± 0.5	-1.9

mond-anvil cell; the ruby method was used to determine the pressure. The experimental results were complemented by *ab initio* density functional calculations using a plane-wave method. Details of the calculation are given in [68, 75], those of the experiment in [76].

The pressure dependence of the various zone center modes in GaN and AlN are given in Fig. 17 together with the results of the calculation. The overall agreement is quite good, in particular the shapes and the curious behavior of the E<sub>2</sub>(low) mode which has a small positive (zero-theory) in AlN and even a negative slope in GaN. The evaluation of the data leads to the pressure derivatives  $\partial\omega/\partial P$  and Grüneisen parameters

$$\gamma = -\partial \ln \omega / \partial \ln V = (B_0 / \omega_0) \partial \omega / \partial P, \quad (8)$$

where  $B_0 = 200$  GPa was taken as a bulk modulus for GaN [30] and 208 GPa for AlN [77]. Our results are summarized in Table 7. Note that the small negative E<sub>2</sub>(low) pressure slopes are reproduced also in the calculations. They were interpreted as being due to a critical balance between central and non-central forces.

The TO–LO splitting has been reported somewhat controversially in the literature. Perlin et al. found that the separation decreased with increasing pressure [78] but had combined data taken on different samples. Our results, shown in Fig. 18, display an increase in splitting and hence effective charge, and they were recorded on the same sample making them somewhat more reliable.

The pressure slopes of hexagonal GaN and AlN as well as of cubic GaN are summarized in Table 8 together with the derived theoretical values. They, too, show a reasonable agreement. Different from, e.g. GaAs, the effective charge changes only little under hydrostatic pressure, which we believe is a consequence of the strong directional covalent bonding of the nitrides; they behave similar to SiC or diamond but less pronounced.

**4 Conclusion** In summary we presented a review of our work on the lattice dynamics of group-III nitrides. With first-order Raman spectroscopy we determined the zone-center phonons of GaN and AlN and their dependence on structural properties. Our investigations on the angular dispersion of the polar A<sub>1</sub> and E<sub>1</sub> modes confirmed the theory, that in case of larger TO–LO splitting compared to the A<sub>1</sub>–E<sub>1</sub> splitting the angular dependent quasi modes are still pure transverse or longitudinal with mixed symmetry. We showed details of the strain distribution of different GaN samples and added experimental data about coupled LO phonon plasmon modes (LPP modes) in the lower frequency range, i.e. the dependence on carrier densities between 10<sup>18</sup> and 10<sup>19</sup> cm<sup>-3</sup>. Studies on Al<sub>x</sub>Ga<sub>1-x</sub>N samples covering the whole composition range 0 < x < 1 certified the two-mode behavior of the E<sub>2</sub>(high) phonon and revealed the same with regard to the A<sub>1</sub>(TO) mode. We analyzed the incorporation of the hexagonal minority phase in cubic GaN samples and presented methods for its quantitative determination. With second-order Raman spectroscopy we measured the frequencies of zone-boundary phonons of hexagonal GaN and AlN as well as cubic GaN in various scattering geometries corresponding to different symmetries. We compared the experimental data with a calculated phonon dispersion and, considering the selection rules obtained from a group-theoretical analysis, discussed the observed phonon modes. Assignments for hexagonal GaN and AlN were given and the behavior under hydrostatic pressure discussed.

**Acknowledgements** The work presented here was done in part in cooperation with F. Bechstedt and K. Syassen. It was furthermore partly supported by the Deutsche Forschungsgemeinschaft. L. Eckey, L. Filippidis, G. Kaczmarczyk, A. Kaschner, A. R. Goñi, and A. P. Litvinchuk promoted this project with their dedicated work. We are very grateful to several growth teams for providing specimens: T. Detchprohm and K. Hiramatsu (Nagoya University), H. Amano and I. Akasaki (Meijo University), D. Schikora, D. J. As and K. Lischka (Universität Paderborn), M. Stutzmann (TU München), O. Briot (Université de Toulouse), D. K. Wickenden (Hopkins University), M. Hommel (Universität Bremen), and J. Pastrňák (former Czechoslovak Academy of Sciences, Prague).

## References

- [1] S. Strite and H. Morkoç, *J. Vac. Sci. Technol. B* **10**(4), 1237 (1992).
- [2] S. Nakamura, T. Mukai, and M. Senoh, *Jpn. J. Appl. Phys. Part 2*, **30**, L1998 (1991).
- [3] S. Nakamura, M. Senoh, S. Nagahama, N. Iwasa, T. Yamada, T. Matsushita, Y. Sugimoto, and H. Kiyoku, *Appl. Phys. Lett.* **69**, 4056 (1996).
- [4] T. N. Oder, J. Li, J. Y. Lin, and H. X. Jiang, *Appl. Phys. Lett.* **77**, 791 (2000).
- [5] H. Morkoç, S. Strite, G. B. Gao, M. E. Lin, B. Sverdlov, and M. Burns, *J. Appl. Phys.* **76**, 1363 (1994).
- [6] C. M. Lueng, H. L. W. Chan, C. Surya, and C. L. Choy, *J. Appl. Phys.* **88**, 5360 (2000).
- [7] K. Naniwae, S. Itoh, H. Amano, K. Itoh, K. Hiramatsu, and I. Akasaki, *J. Cryst. Growth* **99**, 381 (1990).
- [8] T. Detchprohm, K. Hiramatsu, H. Amano, and I. Akasaki, *Appl. Phys. Lett.* **61**, 2688 (1992).
- [9] K. Hiramatsu, T. Detchprohm, and I. Akasaki, *Jpn. J. Appl. Phys.* **32**, 1528 (1993).
- [10] H. Amano, N. Sawaki, I. Akasaki, and Y. Toyoda, *Appl. Phys. Lett.* **48**, 353 (1986).
- [11] I. Akasaki, H. Amano, N. Koide, M. Kotaki, and K. Manabe, *Physica B* **185**, 428 (1993).
- [12] D. J. As, D. Schikora, A. Greiner, M. Lübbes, J. Mimkes, and K. Lischka, *Phys. Rev. B* **54**, R11118 (1996).
- [13] D. Schikora, M. Hankeln, D. J. As, K. Lischka, T. Litz, A. Waag, T. Buhrow, and F. Henneberger, *Phys. Rev. B* **54**, R8381 (1996).
- [14] H. Angerer, O. Ambacher, R. Dimitrov, T. Metzger, W. Rieger, and M. Stutzmann, *MIJ-NSR* **1**, Article 15 (1996).
- [15] H. Angerer, D. Brunner, F. Freudenberger, O. Ambacher, M. Stutzmann, R. Höpler, T. Metzger, E. Born, G. Dollinger, A. Bergmaier, S. Karsch, and H. J. Körner, *Appl. Phys. Lett.* **71**, 1504 (1997).
- [16] J. Pastrňák and L. Roskocová, *phys. stat. sol.* **7**, 331 (1964).
- [17] J. Pastrňák and L. Roskocová, *phys. stat. sol.* **26**, 591 (1968).
- [18] P. Lawaetz, *Phys. Rev. B* **5**, 4039 (1972).
- [19] M. Cardona, in: *Light Scattering in Solids II*, edited by M. Cardona and G. Güntherodt, *Topics Appl. Phys.* **50**, Springer, Berlin, Heidelberg 1982 (p. 19ff).
- [20] D. D. Manchon, Jr., A. S. Barker, Jr., P. J. Dean, and R. B. Zetterstrom, *Solid State Commun.* **8**, 1227 (1970).
- [21] A. Cingolani, M. Ferrara, M. Lugara, and G. Scamarcio, *Solid State Commun.* **58**, 823 (1986).
- [22] P. Perlin, C. Jaubertie-Carillon, J. P. Itie, A. San Miguel, I. Grzegory, and A. Polain, *Phys. Rev. B* **45**, 83 (1992).
- [23] T. Azuhata, T. Sota, K. Suzuki, and S. Nakamura, *J. Phys. C* **7**, L129 (1995).
- [24] L. E. McNeil, M. Grimsditch, and R. H. French, *J. Am. Ceram. Soc.* **76**, 1132 (1993).
- [25] R. Loudon, *Adv. Phys.* **13**, 423 (1964).
- [26] C. A. Arguello, D. L. Rousseau, and S. P. S. Porto, *Phys. Rev.* **181**, 1351 (1969).
- [27] L. Filippidis, H. Siegle, A. Hoffmann, C. Thomsen, K. Karch, and F. Bechstedt, *phys. stat. sol. (b)* **198**, 621 (1996).
- [28] T. Kozawa, T. Kachi, H. Kano, H. Nagase, N. Koide, and K. Manabe, *J. Appl. Phys.* **77**, 4389 (1995).
- [29] F. Demangeot, J. Frandon, M. A. Renucci, O. Briot, B. Gil, and R. L. Aulombard, *Solid State Commun.* **100**, 207 (1996).
- [30] C. Kisielowski, J. Krüger, S. Ruvimov, T. Suski, J. W. Ager III, E. Jones, Z. Lilienthal-Weber, M. Rubin, E. R. Weber, M. D. Bremser, and R. F. Davis, *Phys. Rev. B* **54**, 17745 (1996).
- [31] J.-M. Wagner and F. Bechstedt, *Phys. Rev. B* **66**, 115202 (2002).
- [32] K. Hiramatsu, S. Kitamura, and N. Sawaki, *Mater. Res. Soc. Symp. Proc.* **395**, 267 (1996).
- [33] S. Kitamura, K. Hiramatsu, and N. Sawaki, *Jpn. J. Appl. Phys.* **34**, L1184 (1995).
- [34] H. Siegle, *Dissertation*, Technische Universität Berlin, p. 96 (1998).
- [35] A. Hoffmann, H. Siegle, A. Kaschner, L. Eckey, C. Thomsen, J. Christen, F. Bertram, M. Schmidt, K. Hiramatsu, S. Kitamura, and N. Sawaki, *J. Cryst. Growth* **189/190**, 630 (1998).
- [36] B. B. Varga, *Phys. Rev.* **137**, A1896 (1965).
- [37] A. Mooradian and G. B. Wright, *Phys. Rev. Lett.* **16**, 999 (1966).

- [38] E. Burstein, A. Pinczuk, and S. Iwasa, *Phys. Rev.* **157**, 611 (1967).
- [39] P. Perlin, J. Camassel, W. Knap, T. Taliercio, J. C. Chervin, T. Suski, I. Grzegory, and S. Porowski, *Appl. Phys. Lett.* **67**, 2524 (1995).
- [40] D. T. Hon and W. L. Faust, *Appl. Phys.* **1**, 241 (1973).
- [41] J. F. Scott, T. C. Damen, J. Ruvalds, and A. Zawadowski, *Phys. Rev. B* **3**, 1295 (1971).
- [42] M. V. Klein, B. N. Ganguly, and P. J. Colwell, *Phys. Rev. B* **6**, 2380 (1972).
- [43] R. Rupp and J. Nahum, *J. Phys. Chem. Solids* **75**, 1311 (1974).
- [44] T. Kozawa, T. Kachi, H. Kano, Y. Taga, M. Hashimoto, N. Koide, and K. Manabe, *J. Appl. Phys.* **75**, 1098 (1994).
- [45] F. A. Ponce, J. W. Steeds, C. D. Dyer, and G. D. Pitt, *Appl. Phys. Lett.* **69**, 2650 (1996).
- [46] F. Demangeot, J. Frandon, M. A. Renucci, C. Meny, O. Briot, and R. L. Aulombard, *J. Appl. Phys.* **82**, 1305 (1997).
- [47] H. Siegle, A. Hoffmann, L. Eckey, C. Thomsen, J. Christen, F. Bertram, D. Schmidt, D. Rudloff, and K. Hiramatsu, *Appl. Phys. Lett.* **71**, 2490 (1997).
- [48] M. Drechsler, D. M. Hofmann, B. K. Meyer, T. Detchprohm, H. Amano, and I. Akasaki, *Jpn. J. Appl. Phys.* **34**, L1178 (1995).
- [49] R. Besermann, C. Hirlmann, M. Balkanski, and J. Chevalier, *Solid State Commun.* **20**, 485 (1976).
- [50] B. Jusserand and S. Slempek, *Solid State Commun.* **49**, 95 (1984).
- [51] S. Emura, S. Gonda, Y. Matsui, and H. Hayashi, *Phys. Rev. B* **38**, 3280 (1988).
- [52] X. Wang and X. Zhang, *Solid State Commun.* **59**, 869 (1986).
- [53] K. Hayashi, K. Itoh, N. Sawaki, and I. Akasaki, *Solid State Commun.* **77**, 115 (1991).
- [54] A. Cros, H. Angerer, O. Ambacher, R. Höpler, T. Metzger, and M. Stutzmann, *Solid State Commun.* **104**, 35 (1997).
- [55] K. Karch, F. Bechstedt, and T. Pletl, *Phys. Rev. B* **56**, 3560 (1997).
- [56] S. Strite, M. E. Lin, and H. Morkoç, *Thin Solid Films* **231**, 197 (1993).
- [57] T. Lei, K. F. Ludwig, Jr., and T. D. Moustakas, *J. Appl. Phys.* **74**, 4430 (1993).
- [58] O. Brandt, H. Yang, B. Jenichen, Y. Suzuki, L. Däweritz, and K. H. Ploog, *Phys. Rev. B* **52**, R2253 (1995).
- [59] H. Siegle, L. Eckey, A. Hoffmann, C. Thomsen, B. K. Meyer, D. Schikora, M. Hankeln, and K. Lischka, *Solid State Commun.* **96**, 943 (1995).
- [60] C. Thomsen, R. Wegerer, H.-U. Habermeier, and M. Cardona, *Solid State Commun.* **83**, 199 (1992).
- [61] S. Miyoshi, K. Onabe, N. Ohkouchi, H. Yaguchi, R. Ito, S. Fukatsu, and Y. Shiraki, *J. Cryst. Growth* **124**, 439 (1992).
- [62] M. Giehler, M. Ramsteiner, O. Brandt, H. Yang, and K. H. Ploog, *Appl. Phys. Lett.* **67**, 733 (1995).
- [63] S. Murugkar, R. Merlin, A. Botchkarev, A. Salvador, and H. Morkoç, *J. Appl. Phys.* **77**, 6042 (1995).
- [64] H. Siegle, L. Filippidis, G. Kaczmarczyk, A. P. Litvinchuk, A. Hoffmann, and C. Thomsen, in: *Proceedings of the 23<sup>rd</sup> International Conference on Physics of Semiconductors (ICPS 23)*, Berlin, Germany, World Scientific 1996 (p. 533 ff).
- [65] H. Siegle, G. Kaczmarczyk, L. Filippidis, A. P. Litvinchuk, A. Hoffmann, and C. Thomsen, *Phys. Rev. B* **55**, 7000 (1997).
- [66] E. O. Kane, *Phys. Rev. B* **31**, 7865 (1985).
- [67] K. Karch and F. Bechstedt, *Phys. Rev. B* **56**, 7404 (1997).
- [68] K. Karch, J.-M. Wagner, and F. Bechstedt, *Phys. Rev. B* **57**, 7043 (1998).
- [69] T. Ruf, J. Serrano, M. Cardona, P. Pavone, M. Pabst, M. Krisch, M. D'Astuto, T. Suski, I. Grzegory, and M. Leszczynski, *Phys. Rev. Lett.* **86**, 906 (2001).
- [70] V. Yu. Davydov, Yu. E. Kitaev, I. N. Goncharuk, A. N. Smirnov, J. Graul, O. Semchinova, D. Uffmann, M. B. Smirnov, A. P. Mirgorodsky, and R. A. Evarestov, *Phys. Rev. B* **58**, 12899 (1998).
- [71] J. M. Zhang, T. Ruf, M. Cardona, O. Ambacher, M. Stutzmann, J.-M. Wagner, and F. Bechstedt, *Phys. Rev. B* **56**, 14399 (1997).
- [72] I. Gorczyca, N. E. Christensen, E. L. Peltzer y Blancá, and C. O. Rodriguez, *Phys. Rev. B* **51**, 11936 (1995).
- [73] Z. X. Liu, A. R. Goñi, K. Syassen, H. Siegle, C. Thomsen, B. Schöttker, D. J. As, and D. Schikora, *J. Appl. Phys.* **86**, 929 (1999).
- [74] G. Kaczmarczyk, A. Kaschner, A. Hoffmann, and C. Thomsen, *Appl. Phys. Lett.* **78**, 198 (2001).
- [75] J.-M. Wagner and F. Bechstedt, *Phys. Rev. B* **62**, 4526 (2000).
- [76] A. R. Goñi, H. Siegle, K. Syassen, C. Thomsen, and J.-M. Wagner, *Phys. Rev. B* **64**, 035205 (2001).
- [77] M. Ueno, A. Onodera, O. Shimomura, and K. Takemura, *Phys. Rev. B* **45**, 10123 (1992).
- [78] P. Perlin, T. Suski, J. W. Ager III, G. Conti, A. Polian, N. E. Christensen, I. Gorczyca, I. Grzegory, E. R. Weber, and E. E. Haller, *Phys. Rev. B* **60**, 1480 (1999).